

CARBON BASED ANODE MATERIALS FOR SODIUM ION BATTERIES



**A thesis submitted
in partial fulfilment of the requirements for the
BS-MS Dual Degree Programme
by**

Alma Mathew

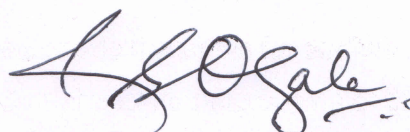
(20131059)

**Under the guidance of
Prof. Satishchandra B Ogale**

**Indian Institute of Science Education and Research
Dr.Homi Bhabha Road, Pashan,
Pune 411008, India.**

Certificate

This is to certify that the dissertation titled "Carbon based anode materials for sodium ion batteries" towards the partial fulfilment of the BS-MS dual degree programme at the Indian Institute of Science Education and Research, Pune represents the study carried out by Alma Mathew at Indian Institute of Science Education and Research under the supervision of Prof. Satishchandra B Ogale, Professor, Department of Physics during the academic year 2017-2018.



Prof. Satishchandra B Ogale

Professor

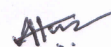
Committee:

Prof. Satishchandra B Ogale (Supervisor)

Dr. Muhammed Musthafa O T (TAC)

Declaration

I hereby declare that the matter embodied in the report titled "Carbon based anode materials for sodium ion batteries" are the results of the work carried out by me at the Department of Physics, Indian Institute of Science Education and Research, Pune, under the supervision of Prof. Satishchandra B Ogale and the same has not been submitted elsewhere for any other degree.



Alma Mathew

20131059

Dedicated to my family

Acknowledgment

I extend my wholehearted gratitude to my mentor, Prof. Satishchandra B Ogale for his excellent guidance, constant encouragement and also for his valuable suggestions and pieces of advice at numerous times.

I specially thank Dr. Malik Wahid, Dr. Dhanya Puthussery, Apurva Lohgaonkar, Ankur Singh, Kingshuk Roy, Neha Sharma, Nagaraj N M and all other SBO lab members for their immense help towards successfully completing my project. I equally thank Debanjan Chakraborty for his great help in obtaining BET data.

I extremely thank my friends, Anjana and Swathi, without their support the past one year wouldn't have been imaginable.

I most importantly thank my family members who have been encouraging and supporting me all throughout the journey, special mention to my Amma for listening, understanding, for all the love and care you have given throughout.

I also thank Raman and SEM operators for the help in acquiring various data.

I'm also grateful to the Department of Science and Technology, India for the INSPIRE fellowship. I also thank all IISER Pune members who have been helping by different means.

Abstract

Sodium ion batteries are being investigated as a substitute for lithium ion batteries due to the limited availability of lithium resources in Earth's crust. Hard carbon with interplanar distance greater than graphite is suitable for sodium ion intercalation and de-intercalation. In the present study, two types of carbonaceous materials have been investigated for its application in sodium ion battery anode.

Melamine-formaldehyde resin and sugarcane bagasse and its composites were pyrolyzed at 800 °C in Argon atmosphere. The carbonized products obtained showed an interplanar distance in the range of 0.34 to 0.38 nm. The sodium ion storage in the composite is analyzed by galvanostatic charge-discharge measurements at a current density of 100 mA g⁻¹.

Pyrolysis of mustard seeds at 800 °C under Argon atmosphere for 6 hours was carried out to obtain carbonized product. The hard carbon formed showed a surface area of 28 m² g⁻¹. This hard carbon shows a capacity of 142 mA h g⁻¹ at 100 mA g⁻¹ with good cycling stability up to 270 cycles.

List of tables

No.	Title	Page no.
3.1.1	Summary of XRD analysis of bagasse-resin samples	29
3.1.2	Summary of Raman analysis of bagasse-resin samples	31
3.1.3	BET surface area of bagasse- resin samples	32
3.2.1	XRD analysis of mustard sample	34
3.2.2	Raman spectrum of mustard sample	35
3.2.3	BET surface area of mustard sample	36

List of illustrations

No.	Title	Page no.
1.2	Schematic representation of working of a SIB	14
1.3	Schematic representations of soft carbon, hard carbon and graphite	16
2.3.1	Schematic representation of X-ray diffraction from crystal planes	19
2.3.2.1	Schematic representation of possible scatterings	20
2.3.2.2	Schematic representation of the Raman spectrometer	20
2.3.3	Schematic of a FE-SEM	22
2.3.4	Schematic representation for BET surface area measurement	24
2.4	Schematic illustration of assembly of a coin cell	25
2.5.1	Circuit diagram for the measurement of cyclic voltammetry	26
3.1.1	XRD patterns of the carbonized samples	29
3.1.2	Raman spectra of carbonized bagasse - resin samples	30
3.1.3	SEM images of i) 0B 100R ii) 25B 75R iii) 50B 50R iv) 75B 25R v) 100B 0R	31
3.1.4	i) Charge-discharge profile of 50B 50R sample ii) Stability curve of 50B 50R sample up to 50 cycles	33
3.2.1	XRD pattern from carbonized mustard sample	34
3.2.2	Raman spectrum of mustard sample	35
3.2.3	SEM image of mustard sample	35
3.2.4	CV plot in the range 0.01- 3V vs. Na/Na ⁺	36
3.2.5	Electrochemical performance of mustard sample	37
3.2.6	i) Charge – discharge profile of mustard sample ii) Stability curve of mustard sample up to 270 cycles	38

Abbreviations

LIB – Lithium ion battery

SIB – Sodium ion battery

EC – Ethylene carbonate

PC – Propylene carbonate

DMC – Dimethyl carbonate

FEC - Fluoro ethylene carbonate

ES - Ethylene sulfite

VC - Vinylene carbonate

DFEC - Difluoro ethylene carbonate

SEI - Solid electrolyte interface

PVDF - Polyvinylidene fluoride

NMP - N-Methyl-2-pyrrolidone

XRD – X-ray Diffraction

IR – Infra red

FE-SEM – Field Emission Scanning Electron Microscopy

EDX – Energy Dispersive X-ray Analysis

BET - Brunauer–Emmett–Teller

DFT – Density Functional Theory

CV – Cyclic Voltammetry

EIS - Electrochemical impedance spectroscopy

FWHM – Full width at half maximum

CONTENTS

1 Introduction	12
1.1 Historical development in batteries	12
1.2 Working principle of sodium ion battery.....	13
1.3 Carbon based anode materials.....	15
2 Materials and methods	17
2.1 Chemicals and materials.....	17
2.2 Synthesis.....	17
2.2.1 Carbon from bagasse and melamine-formaldehyde resin.....	17
2.2.1.1 Carbon from sugarcane bagasse.....	17
2.2.1.2 Carbon from melamine – formaldehyde resin.....	17
2.2.1.3 Carbon from composites of sugarcane bagasse and melamine- formaldehyde resin.....	18
2.2.2 Carbon from pyrolysis of mustard seed.....	18
2.3 Physical and chemical characterization techniques.....	18
2.3.1 X-ray diffraction.....	18
2.3.2 Raman spectroscopy.....	19
2.3.3 Field Emission Scanning Electron Microscopy and Energy Dispersive X- ray Analysis.....	21
2.3.4 Brunauer–Emmett–Teller N ₂ adsorption.....	23
2.4 Electrode and coin cell fabrication.....	24
2.5 Electrochemical characterization techniques.....	25
2.5.1 Cyclic voltammetry.....	25
2.5.2 Galvanostatic charge-discharge measurement.....	26

3 Results and discussion	28
3.1 Carbon from bagasse and melamine-formaldehyde resin.....	28
3.1.1 Physical and chemical characterization.....	28
3.1.2 Electrochemical characterization.....	32
3.2 Carbon from pyrolysis of mustard seed.....	33
3.2.1 Physical and chemical characterization.....	33
3.2.2 Electrochemical characterization.....	36
4 Conclusion and future aspects	39
References	40

Chapter 1

INTRODUCTION

The rising global temperature and the changes in climate starting from the beginning of 20th century are currently the hot topics in this era. Exploitation of non-renewable energy resources such as fossil fuels has resulted in a major contribution to global warming and greenhouse effect. The energy crisis and increasing global energy consumption demand the use of renewable sources of energy. Among the renewable energy sources, there are limitations such as time and weather for wind, solar and hydropower energy. Therefore, conversion and storage of electrical energy in sustainable and eco-friendly systems is of greater importance. In the existing energy storage systems, batteries, generally called electrochemical cells have gained significant attention due to its high energy density, rate performance, cycling stability, safety and its applications in electric vehicles and portable electronic devices.

1.1 Historical development in batteries

Batteries are among the major research topics as the need for energy storing systems are in increasing demand. Batteries are classified into two, primary batteries and secondary batteries. Primary batteries stop functioning once the supply of reactants is over and the chemical reaction cannot be reversed. On the other hand, secondary batteries can be charged and discharged for several cycles, and the chemical reactions can be reversed by applying an electric current. The chemical reactions at the anode and cathode are converted to electrical energy when potential is applied. Reaction at anode takes place at a lower potential whereas at cathode the potential required is higher.

In 1748, Benjamin Franklin coined the term battery for a set of capacitors he used for experiments with electricity. Alessandro Volta, an Italian physics professor in 1800, made the first electrochemical cell and the studies of rechargeable batteries initiated by the discovery of the lead-acid battery in 1899. Later on, nickel cadmium and nickel-iron

batteries were invented. By 1990, commercialization of nickel-metal hydride batteries was started due to their good capacity, power density, better environmental tolerance and cost. In the 1970s the studies on Li ions as charge carriers in an electrochemical cell were initiated and in 1980, John B Goodenough, an American chemist developed a lithium-containing transition metal oxide LiCoO_2 , as a positive electrode for lithium-ion batteries (LIBs). In 1991, Sony Co started the commercialization of LIBs with LiCoO_2 as cathode material and graphite as anode material. Commercialization of LIBs was followed by lithium-ion polymer batteries in 1999 and nano phosphate lithium-ion batteries in 2001.^[1] The limited availability of lithium resources in the Earth's crust demands to look into other metals with high Earth abundance such as sodium which could make a better alternative for lithium-ion batteries. Therefore, studies on sodium containing layered oxides were conducted, and sodium ion batteries (SIBs) are extensively being studied. Similar to LIBs where lithium gets inserted into the graphitic anode, in SIBs the mechanism of sodium intercalation into hard carbon was investigated by Stevens and Dahn.^[2] Currently, extensive research has been focused on hard carbon and its application as an anode material in SIB.

Batteries which can deliver highest energy density are of greater importance. LIBs dominate among the batteries which can deliver higher energy density. Since lithium has the lowest reduction potential, it can operate at a high operating voltage 3.6 - 3.8 V and can function at wide ranges of temperature has made LIB popular.^[3] Also, lithium has advantages like light-weight, low maintenance and low self-discharge.^[4] On a long run, the cost of LIBs and shortage of some of the transition metals used in LIBs will be a problem shortly. Therefore, it is found that among the electrochemical energy storage devices, SIBs with the similar chemistry of that of LIBs are promising and can replace the commercially available LIBs.

1.2 Working principle of sodium ion battery

Figure 1.2 shows the working principle of SIBs. SIBs show a similar working principle as that of LIBs. Sodium ion shuttles between the anode and cathode material through electrolyte. During discharge of a battery, electrons are released from anode to cathode by an external circuit to maintain the electric charge while the sodium ion moves to the

cathode. While charging, sodium ion moves back to the anode through electrolyte and reverse flow of electrons occur through the external circuit. Sodium ion functions as the charge carrier. The most common used electrolytes for SIBs are sodium salts such as NaClO_4 , NaPF_6 or NaCF_3SO_3 dissolved in organic solvents dimethyl carbonate (DMC), propylene carbonate (PC), ethylene carbonate (EC).^[5] Electrolyte must be electrically insulating and ionically conducting. An electrolyte contributes to the stability of an electrochemical cell. Generally, electrolyte additives such as fluoro ethylene carbonate (FEC), ethylene sulfite (ES), vinylene carbonate (VC) and difluoro ethylene carbonate (DFEC) are found to be efficient electrolyte additives for the stable solid electrolyte interface (SEI) layer formation and to improve the electrochemical stability.^[6] The separator prevents the direct contact between anode and cathode.

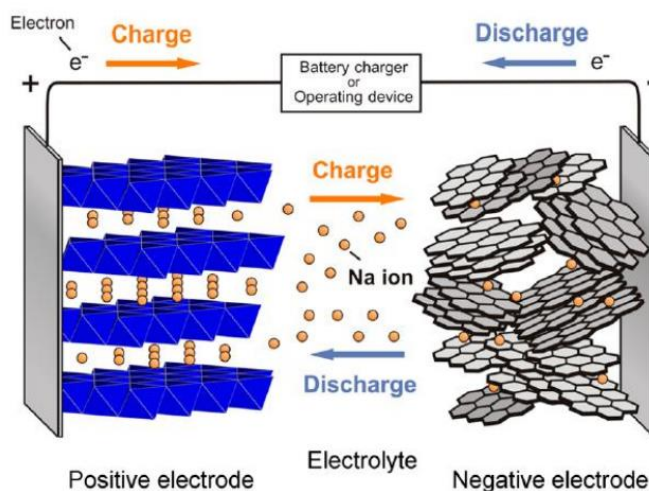


Figure 1.2 Schematic representation of working of a SIB ^[6]

Cathode and anode materials play a major role in the energy density, capacity, cyclic stability and safety. A cathode material must be chosen such that it must be stable for the repeated intercalation and de-intercalation of sodium ions in high voltage range. Also, the cathodic reactions occur at high potential relative to the reference (Na/Na^+) electrode. Good electronic conductivity, high capacity to host the incoming sodium ions, stability over several charge-discharge cycles and low cost are required for an excellent cathode material. A wide variety of compounds have been studied for cathode material in SIBs. Sodium-containing layered transition metal oxides such as NaFeO_2 , NaMnO_4 ,

NaCoO_2 , NaNiO_2 similar to that of LiCoO_2 , the positive electrode used in commercial LIBs are found to be promising cathode materials in SIBs. Similarly, layered transition metal phosphates, pyrophosphates and mixed fluorides and organic compounds like $\text{Na}_3\text{V}_2(\text{PO}_4)_2\text{F}_3$ and $\text{NaV}_2(\text{PO}_4)_3$ are found to be better cathode materials for SIBs.^[7]

Likewise, extensive research is carried out for superior anode materials for SIBs. The requirements for an anode material are i) potential at which sodium intercalation and de-intercalation happen must be low ii) high specific capacity to accommodate maximum sodium ions iii) material must be stable for repeated sodiation and de-sodiation iv) low cost and safety. Broad choice of anode materials like carbon-based materials, metal oxides, metal phosphates, phosphorous-based materials, and alloys based on sodium is found to be efficient as anodes for SIBs. However, the huge volume expansion of the sodium based alloy materials during sodiation and long-term stability issues has restricted to commercialize it as anode materials. The abundance, low cost, high cycling stability, ease of synthesis, high safety and the ability to react with lithium and sodium at very low potential has made carbon as an excellent negative electrode material.^[8] In addition, carbon based materials with high surface area is known to be promising for supercapacitor electrodes as well.

1.3 Carbon based anode materials

Carbonaceous materials have been broadly studied for its application as an anode material for SIBs. Graphite, the commercialized anode material for the lithium-ion battery is not suitable for SIB as the ionic size of Na (1.02 Å) is higher than Li (0.76 Å), and graphite interplanar spacing is not appropriate to accommodate Na ions. Therefore, the focus has turned to hard carbons which are well suited for the sodium ions due to the random alignment of graphene layers and enhanced d-spacing.

There are three classes of carbons which are commercially important for batteries. Figure 1.3 represents the three carbons namely, soft carbon, hard carbon and graphite. Pure graphite consists of hexagonally packed planes of carbon atoms stacked horizontally with a distance of 3.35 Å between the graphene layers. During the pyrolysis of precursors, if the remaining carbon atoms after decomposition align into

planar, semi-fluid, parallel sheet-like structures, which on heating to higher temperature yield more graphitization, it is called soft or graphitizable carbon.^[9] Hard carbons are commonly obtained from solid-state pyrolysis of organic polymers and biomass in which the carbon atoms are randomly oriented and there is no significant in-plane ordering.^[4] Soft carbons have significantly high electronic conductivity and high rate capability.^[10] Due to high surface area of soft carbons, they have a high irreversible capacity loss. It causes ion trapping into nanopores which can only be taken at very low operating currents. This reduces the energy density of the cell and cause poor rate capability and capacity fading. Hard carbons have high cycling stability and high specific capacity when compared to soft carbons.^[11] But less electronic conductivity of hard carbon compared to soft carbon causes local high-density current flow which effects in capacity fading. It also has low energy and power density which limit its practical applications.

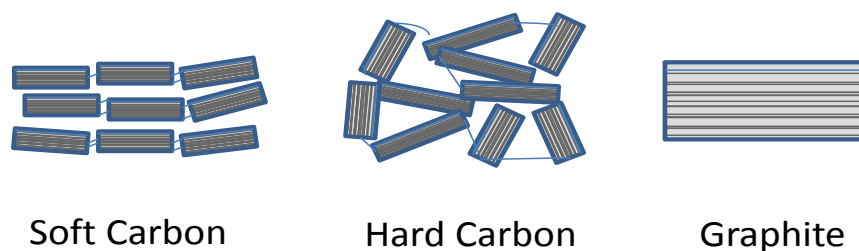


Figure 1.3 Schematic representations of soft carbon, hard carbon and graphite

In the present study, we aim to synthesize and characterize two types of carbonaceous materials and physically mix them at different compositions to learn the chemical and physical characteristics and electrochemical performance of the individual materials and to compare the change in characteristics in the composites. Also, a biomass-derived carbon material was studied for its application in SIBs.

Chapter 2

MATERIALS AND METHODS

2.1 Chemicals and materials

Reagents and compounds used for reactions were purchased from Sigma-Aldrich. Chemicals used are melamine, formaldehyde, H₂SO₄, HCl, PVDF, conducting carbon, NMP, ethylene carbonate, dimethyl carbonate, NaClO₄, fluoroethylene carbonate and sodium metal. Sugarcane bagasse and mustard seeds were used as carbon sources.

2.2 Synthesis

2.2.1 Carbon from bagasse and melamine-formaldehyde resin

2.2.1.1 Carbon from sugarcane bagasse ^[12] (100B 0R)

The sugarcane bagasse was crushed in a mixer to get small pieces. 3g of crushed sugarcane bagasse was mixed properly in an autoclave with 2M H₂SO₄ (10.87 mL H₂SO₄, 98%, and 89.13 mL distilled water). This solution mixture was hydrothermally treated at 180°C for 20 hours. The resultant black mass was centrifuged several times with distilled water and was dried at 100°C for 12 hours. The hydrothermal product was pyrolyzed at 800°C for 6 hours in Argon atmosphere. The pyrolyzed product was stirred overnight in 1M HCl and was centrifuged with distilled water till the pH was neutral.

2.2.1.2 Carbon from melamine – formaldehyde resin ^[13] (0B 100R)

9 mL formaldehyde and 200 mL distilled water was heated to 80°C in a round-bottomed flask. 2.5 g melamine was added to it with stirring. When melamine was entirely dissolved, 2.3 mL formic acid was added to it and kept for 12 hours. The suspension was cooled to room temperature and the solution was rotaevaporated to get the product. The product was pyrolyzed at 800°C for 6 hours in Argon atmosphere.

2.2.1.3 Carbon from composites of sugarcane bagasse and melamine formaldehyde resin

Three composites were synthesized at different proportions (25% Bagasse 75% Resin (25B 75R), 50% Bagasse 50% Resin (50B 50R) and 75% Bagasse 25% Resin (75B 25R)). The already prepared hydrothermal bagasse product was mixed with melamine and formaldehyde mixture and was heated and stirred for 12 hours and was rotaevaporated to get the final product. These composites were pyrolyzed in Argon atmosphere at 800°C for 6 hours. The pyrolyzed product was stirred overnight in 1M HCl and was centrifuged with distilled water till the pH was neutral.

2.2.2 Carbon from pyrolysis of mustard seed

20g mustard seeds were pyrolyzed at 800°C for 4 hours in Argon atmosphere. The sample was ball milled at 400 rpm for 12 hours in Argon atmosphere to get fine powders. The carbonized product was stirred overnight in 1M HCl and was centrifuged with distilled water till the pH reached neutral.

2.3 Physical and chemical characterization techniques

2.3.1 X-ray diffraction

X-ray is an electromagnetic radiation in the wavelength range of 0.01nm to 10 nm. X-rays are used for the determination of the atomic and molecular structure of crystals, lattice parameters, grain size, etc. X-rays are typically used for determination of crystal structure because the order of magnitude of the wavelength of X-ray is similar to that of the interplanar distance of atoms.

The incident X-ray beam from a source is diffracted to different directions based on the density of electron cloud within the crystal structure. The diffracted beam of X-ray undergoes constructive and destructive interference. The X-ray waves cancel each other during destructive interference and get added up during constructive interference. The detector detects the constructively interfered beams using Bragg's law

$$n\lambda = 2d \sin\theta$$

n- order of the diffraction

λ - wavelength of the incident X-ray beam

d- interplanar distance

θ - the angle of incidence

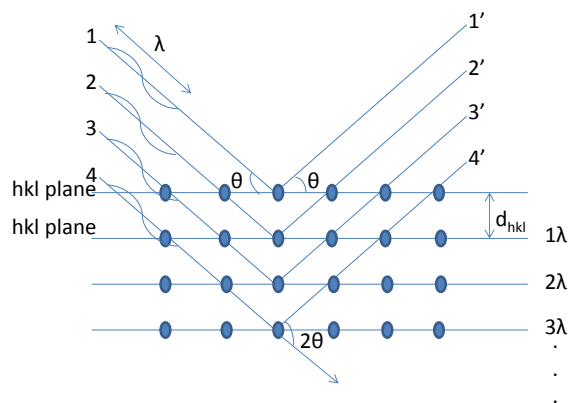


Figure 2.3.1 Schematic representation of X-ray diffraction from crystal planes

Figure 2.3.1 illustrates the X-ray diffraction from crystal planes of the material. By scanning through all possible 2θ angles, different directions of diffractions are obtained depending on the size of the unit crystal of the material. The carbonized products were examined by X-Ray Diffraction (XRD) using a Bruker D8 Advance X-ray Diffractometer equipped with $\text{CuK}\alpha$ radiation with wavelength 1.54178 \AA .

2.3.2 Raman spectroscopy

Raman spectroscopy is used to observe the low-frequency vibrational modes and rotational modes in a system. Raman spectroscopy calculates the change in polarizability of the electron cloud in a molecule and thereby providing a structural fingerprint for a definite molecule. Similar to Raman spectroscopy, infra-red (IR) spectroscopy also gives information about vibrational spectroscopy, even though IR spectroscopy measures the change in net dipole moment of a molecule.

Scattering is of two types. In the dominant elastic scattering or Rayleigh scattering, the energy of the outgoing photon is same as that of incoming photon. However, in inelastic scattering, either the photon loses or gains energy to the scatterer atom or molecule.

Figure 2.3.2.1 represents the possible scattering radiations during both inelastic and elastic scattering.

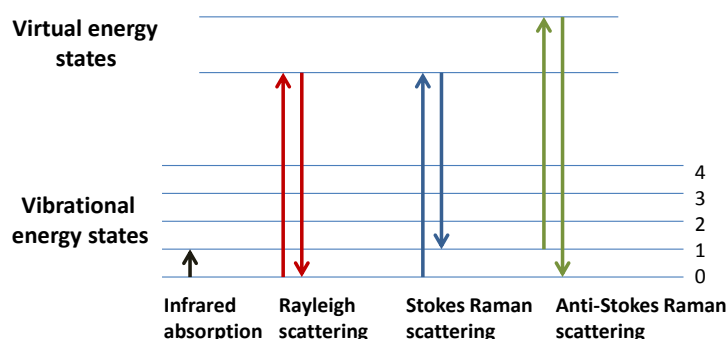


Figure 2.3.2.1 Schematic representation of possible scatterings

Raman scattering can be of two types. Stokes scattering occurs when the energy (or frequency) of the incident photon is more than that of the outgoing photon, whereas in Anti-Stokes Raman scattering, the outgoing photon has a greater frequency than the incoming photon. During Anti-Stokes scattering, the molecule gets excited to a virtual vibrational energy state before relaxation.

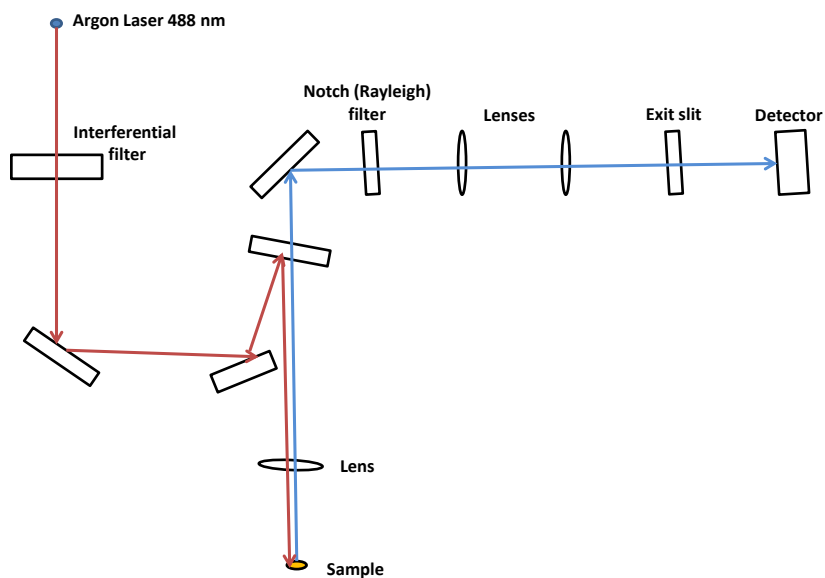


Figure 2.3.2.2 Schematic representation of the Raman spectrometer

Figure 2.3.2.2 represents the schematic representation of a Raman spectrometer. Raman spectra of samples were recorded by using a laser of wavelength 488 nm. A notch filter is used to mask the Rayleigh scattered beam of light. Stokes scattering is

used for analysis of samples. Raman spectroscopy was done using LabRAM HR HORIBA Raman spectrometer with an Argon ion laser of wavelength 488 nm.

2.3.3 Field Emission-Scanning Electron Microscopy and Energy Dispersive Analysis of X-rays

Unlike the use of light in optical microscopes for imaging, in FE-SEM an intense ray of electrons is used to record the images. The equation below shows the de Broglie wavelength, which can be altered by changing the energy of the incoming electron beam.

$$\text{de Broglie wavelength, } \lambda = \frac{h}{\sqrt{(2mE)}}$$

h- Planck's constant

m- mass of an electron

E- kinetic energy of the electron

Therefore, compared to conventional optical microscopes, the spatial resolution from an electron microscope is remarkably higher. Electron microscopes are of two types. Scanning electron microscopes which use the secondary backscattered electrons from the sample for imaging and transmission electron microscope detects the electrons transmitted through the sample for imaging. SEM can provide a minimum resolution up to 1 nm.

Figure 2.3.3 shows the working of a FE-SEM. Samples are sonicated and dispersed in a suitable solvent and then drop cast on to silicon wafer and dried before recording the electron micrographs. Hybrid tungsten- zirconium oxide cathode is used as a source for the thermal field emission. The two anodes and field lenses ensure that the electron beam is properly focused on the sample. Field Emission Scanning Electron Microscope (FE-SEM) images were taken using Zeiss Ultra plus FESEM at a 3kV operating voltage.

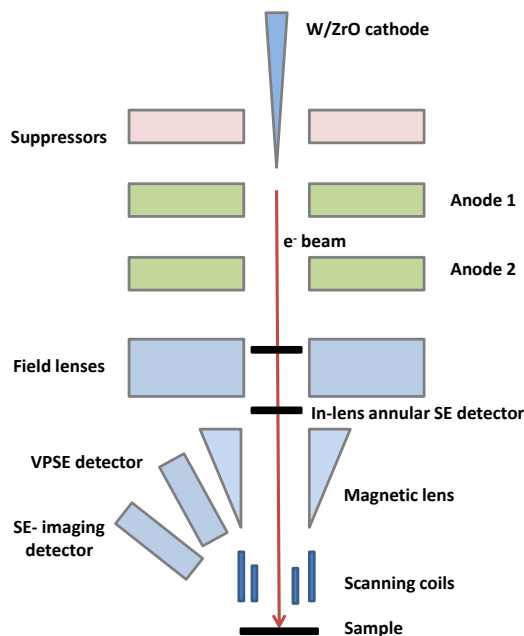


Figure 2.3.3 Schematic of a FESEM

Energy Dispersive Analysis of X-rays (EDX) is a technique for identifying the elemental composition of samples. High energy X-ray or charged particles like electrons or protons is used as a source which is focused on the sample. The unique atomic structure of each element has a unique peak in the X-ray spectrum. The atom which is in ground state gets excited by the incident beam creating a hole in the inner shell. The hole is filled by an electron from a higher energy orbital. The energy difference between the two orbitals is emitted as X-ray. Energy dispersive spectrometer measures the energy of X-ray emitted from the sample.

2.3.4 Brunauer–Emmett–Teller N₂ adsorption

BET model analysis uses adsorption of gas molecules on a solid surface as a basic method for the measurement of pore size or volume and specific surface area of the samples. BET model assumes multilayer adsorption of gas molecules which does not chemically react with the surface of adsorbent. Nitrogen gas is most commonly used and measurements are done at 77K, the boiling point of nitrogen gas. BET theory is developed from Langmuir theory with some basic assumptions such as i) adsorption of gas molecules occurs infinitely in layers ii) gas molecules interact with layers adjacent to

it iii) adsorption of gas molecules follow Langmuir theory at each layer. The BET model multilayer adsorption follows,

$$\frac{1}{v\left[\left(\frac{P}{P_0}\right) - 1\right]} = \frac{c - 1}{v_m c} \left(\frac{P}{P_0}\right) + \frac{1}{v_m c}$$

where,

P- equilibrium pressure of adsorbates

P₀ – saturation pressure of the adsorbates

v – amount of gas adsorbed

v_m – amount gas adsorbed in monolayer

c- BET constant

Amount of gas adsorbed and desorbed with respect to gas pressure at constant temperature is measured separately. Initially, the sample is subjected to heating, normally 100°C, depending on the sample the temperature used for heating is different, and followed by degassing. Further, vacuum is applied to the tubes and the dead volume of the tubes is measured with any inert gas, normally Helium. Vacuum is applied again and addition of nitrogen gas for adsorption measurement is followed. Finally, for desorption measurement nitrogen gas is evacuated. Figure 2.3.4 illustrates the schematic representation for BET surface area measurement. Surface area measurement by Brunauer–Emmett–Teller (BET) technique and pore size distribution of particles by Density Functional Theory (DFT) was done using Quantochrome Autosorb automated gas sorption analyzer.

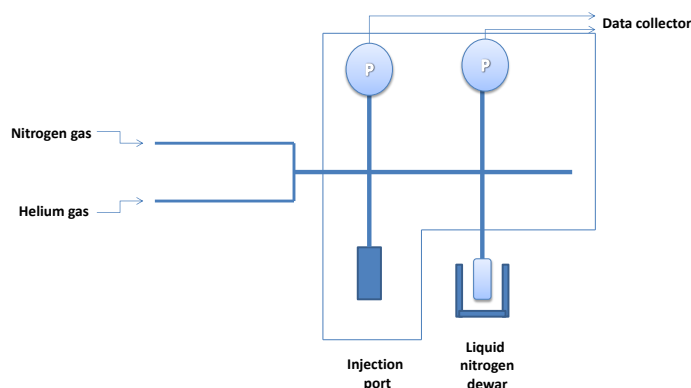


Figure 2.3.4 Schematic representation for BET surface area measurement

2.4 Electrode and coin cell fabrication

10 wt % PVDF binder was properly dissolved in NMP solvent and 20 wt % of conducting carbon followed by 70 wt% of the sample was made into a slurry and coated on a copper foil. The coating was dried overnight at 80⁰C. The circular electrodes were cut using a punching machine suitable for coin cells. Coin cell fabrication was done inside a glove box filled with Argon gas which was maintained at very low oxygen and water content. The half cells were assembled with metallic sodium at one of the sides. A Whatman phase separator filter paper was used to separate the two electrodes. 1M NaClO₄ was dissolved in 1:1 volume ratio of dimethyl carbonate (DMC) and ethylene carbonate (EC) with 2 wt % fluoro ethylene carbonate (FEC) additive previously dissolved in it was used as the electrolyte. Figure 2.4 shows a schematic illustration of a coin cell fabricated in a glove box.

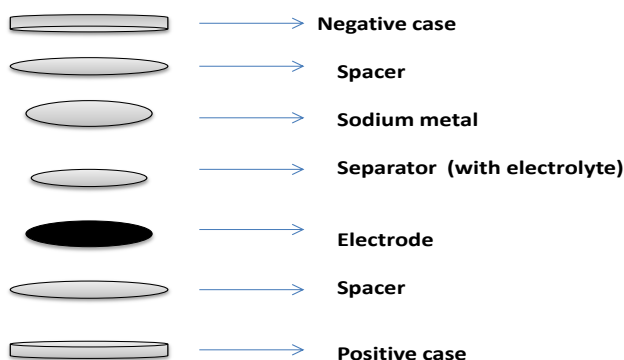


Figure 2.4 Schematic illustration of assembly of a coin cell

2.5 Electrochemical characterization techniques

2.5.1 Cyclic voltammetry

Cyclic voltammetry (CV) is an electrochemical tool used to learn the redox processes of the material of interest. CV measurements are generally performed using a potentiostat where redox active species are scanned at changing potentials. The potentiostat measures the current through the circuit as electrode potential is varied as a function of time. Typically for CV measurements, a three electrode system with a reference electrode, counter electrode and working electrode are used. Here, we used a two electrode system, in an electrochemical cell with sodium metal as the counter electrode. Within a potential range applied between the counter electrode and the working electrode, the resultant current flow is measured with an ammeter. Figure 2.5.1 shows the circuit diagram for this configuration. The plot of current with respect to applied voltage at a particular scan rate is known as a voltammogram. Starting from a very low voltage, say 0.01V, with a potential scan rate of 0.1 mVs^{-1} the current is measured. When the voltage reaches maximum of the applied voltage window, the scanning is reversed and the reverse negative current is measured. CV curve usually shows a hysteresis loop including an anodic peak and a cathodic peak. CV measurements were done using PARSTAT MC automatic measurement system.

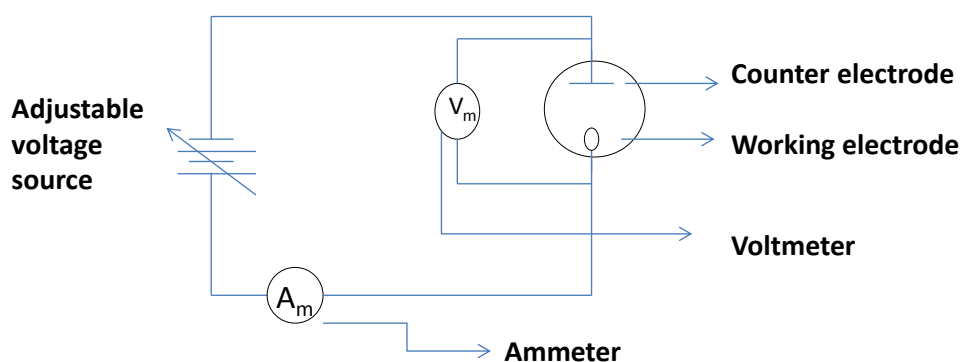


Figure 2.5.1 Circuit diagram for the measurement of cyclic voltammetry

2.5.2 Galvanostatic charge-discharge measurement

Galvanostatic charge- discharge measurements at a constant current density gives information about specific capacity, specific energy and cycling stability in a particular

voltage window. During charge- discharge measurements, a constant current is applied to the electrochemical cell and the cell voltage is measured as a function of time. When the cut-off voltage is reached, the current is reversed.

Capacity is the total amount of electron charge transferred during a charging or discharging process.

Specific charge/discharge capacity,

$$Q = \frac{I * t}{m}$$

where, I- current in mA

t- time in hours

m- mass of active material in grams

Rate capability can also be measured in a similar way by measuring charge- discharge by applying different current densities. Rate capability explains the ability of the active material to retain the capacity at different current densities. Cycling stability gives the number of cycles till which the electrochemical cell is operational. Cycling stability is a plot of specific capacity versus number of cycles. Specific energy is also obtained by multiplying capacity and voltage. The ratio of discharging capacity to the previous charging capacity, coulombic efficiency can provide information about any side reactions that is happening. Coulombic efficiency lower than 100% can lead to capacity loss in an electrochemical cell. The charge- discharge measurements were done in NEWARE automatic battery testing system.

Chapter 3

RESULTS AND DISCUSSION

The compounds synthesized were characterized by different characterization tools and techniques. The phase composition and crystallite size were studied by powder XRD measurements. Raman spectroscopy revealed the extent of graphitization of the carbon samples. SEM and EDX analysis were performed to know about the morphology and elemental compositions of the different samples. BET surface area analysis by N₂ adsorption-desorption provided an idea about the surface area of the samples and pore size distribution were measured by Density Functional Theory. Electrochemical measurements were performed by galvanostatic charge-discharge measurements and cyclic voltammetry.

3.1 Carbon from bagasse and melamine-formaldehyde resin

3.1.1 Physical and chemical characterization

XRD patterns of the pure bagasse (100B 0R), pure resin (0B 100R) and the composites (25B 75R, 50B 50R and 75B 25R) are shown in figure 3.1.1. From the XRD plot, it is observed that there are two broad peaks, a higher intensity peak which corresponds to the family of (002) planes and a lower intensity peak which corresponds to (100) plane.^[14] The very broad peaks indicate the amorphous nature of carbon. Graphite shows a characteristic peak at $2\theta = 26.7^\circ$ which corresponds to (002) plane.^[15] It is observed that there is a gradual shift in peak position towards lower θ values as the amount of bagasse is increased. This observation can be attributed to the increase in interlayer d-spacing according to Bragg's law. The interlayer spacing of the bagasse-resin samples was found to be in a range of 0.34 nm to 0.38 nm. Size of the crystallite particles were calculated using Scherrer formula,

$$\zeta = \frac{K\lambda}{\beta \cos \theta}$$

where, ζ - crystallite size

K - 0.9

λ – 0.15418 nm, wavelength of the X-ray

β – line broadening at full width half maximum (FWHM) in radians

θ – Bragg's angle in degrees

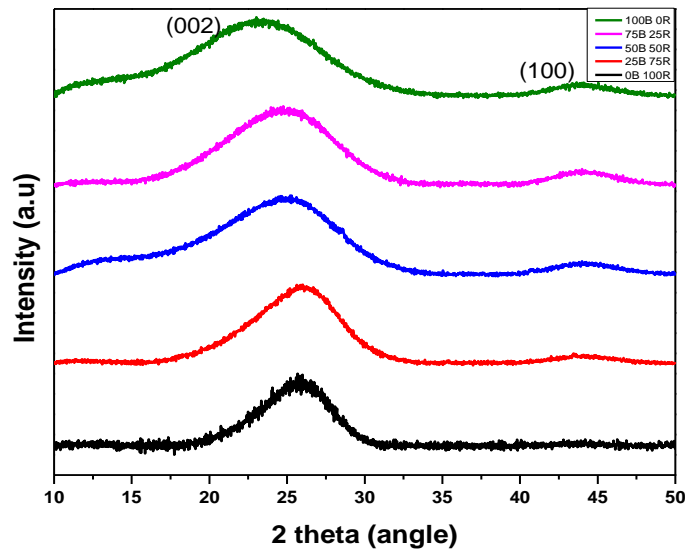


Figure 3.1.1 XRD patterns of the carbonized samples

Sample	XRD peak position (002)/(100)	Interplanar separation (002) (in nm)	in-plane crystallite size (100) (in nm)
0B 100R	25.68 ⁰ / 44.19 ⁰	0.34	3.69
25B 75R	26.01 ⁰ / 43.45 ⁰	0.34	2.78
50B 50R	25.29 ⁰ / 43.99 ⁰	0.35	2.65
75B 25R	24.76 ⁰ / 43.99 ⁰	0.36	3.92
100B 0R	23.01 ⁰ / 43.64 ⁰	0.38	2.26

Table 3.1.1 Summary of XRD analysis of bagasse-resin samples

Samples with interlayer spacing greater than 0.36 nm was reported to be suitable for sodiation and desodiation mechanism in carbon materials.^[16]

Further evaluation of graphitization of the carbon samples were done by Raman spectroscopy. The Raman spectrum shows two prominent peaks. The D-band signifies the defects in the sp^2 hybridized carbon material and G-band indicates the degree of graphitization due to the vibrational modes of sp^3 hybridized carbon in the sample. Figure 3.1.2 demonstrates the Raman spectra for the bagasse-resin samples. Raman spectrum of a defective graphene material shows a G-band positioned at around 1590 cm^{-1} and D-band at around 1320 cm^{-1} .^[17] The samples showed a higher intensity G-band. I_G/I_D ratios were calculated for each sample. Table 3.1.2 shows the G-band and D-band values for bagasse-resin samples and corresponding I_G/I_D ratios. No significant difference in the I_G/I_D ratio was found in the bagasse- resin samples. Even though, 75B 25R sample showed comparatively lower I_G/I_D ratio.

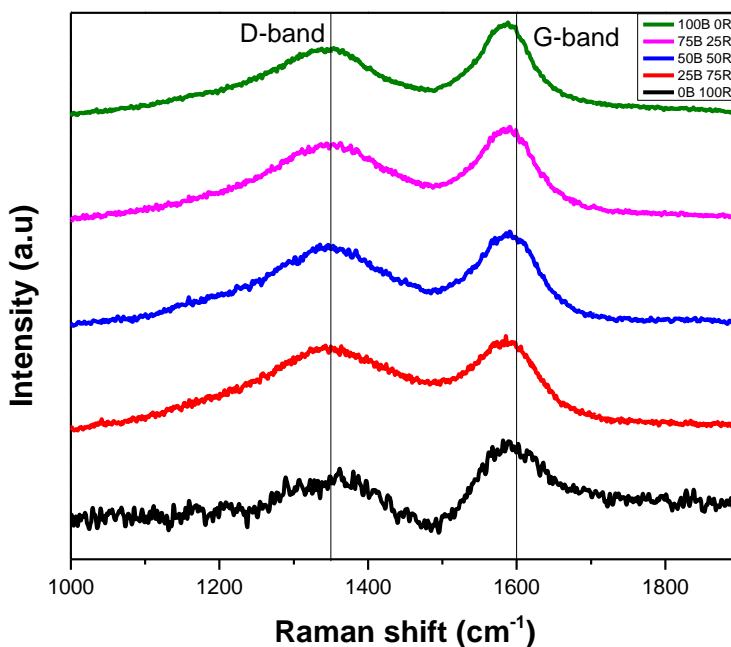


Figure 3.1.2 Raman spectra of carbonized bagasse - resin samples

Sample	Raman G/D band position	Raman I_G/I_D ratio
0B 100R	1594/1353 cm^{-1}	1.17
25B 75R	1585/1342 cm^{-1}	1.18
50B 50R	1590/1335 cm^{-1}	1.19
75B 25R	1590/1363 cm^{-1}	1.16
100B 0R	1588/1353 cm^{-1}	1.17

Table 3.1.2 Summary of Raman analysis of bagasse-resin samples

Figure 3.1.3 shows the morphologies of the bagasse-resin samples obtained by FE-SEM. Samples 75B 25R and 100B 0R showed similar morphology with layered sheet like structures, which is also evident from BET surface area values. The pure resin sample showed a structure with negligible pores in the material.

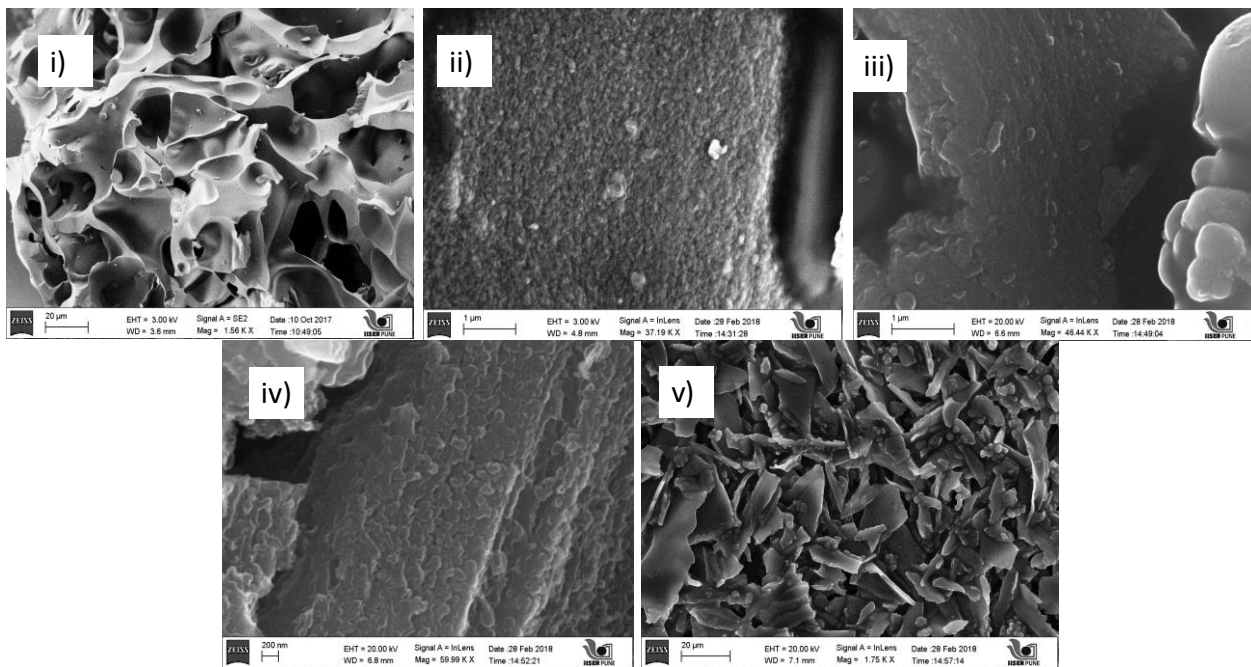


Figure 3.1.3 SEM images of i) 0B 100R ii) 25B 75R iii) 50B 50R iv) 75B 25R v) 100B 0R

The BET surface area of the bagasse-resin samples shows an increasing value as the amount of bagasse in the sample is increased. The table 3.1.3 shows the BET surface area value of each sample. BET surface area of 50B 50R sample is expected to be in

between that of 25B 75R and 75B 25R. But, due to instrumental error the actual surface area value could not be calculated. 0B 100R sample showed the lowest surface area of $35\text{m}^2/\text{g}$, which is an expected value for hard carbon. Hard carbons with a very low surface area are suitable for SIBs due to the development of solid electrolyte interphase (SEI) over a small area, which leads to lower amount of degradation of electrolyte and low irreversible capacity loss.^[18]

Sample	BET surface area (m^2g^{-1})
0B 100R	35
25B 75R	288
50B 50R	-
75B 25R	402
100B 0R	406

Table 3.1.3 BET surface area of bagasse- resin samples

3.1.2 Electrochemical characterization

Among the five samples, the intermediate sample 50B 50R was chosen for the basic electrochemical characterizations. The characterizations of the 50B 50R sample were studied in a sodium ion half- cell configuration. Galvanostatic charge-discharge measurements at a current density of $100\text{mA}\text{g}^{-1}$ showed an initial discharge capacity of $421\text{mA}\text{h}\text{g}^{-1}$. Figure 3.1.4 shows the charge-discharge and stability curve up to 50 cycles. The specific capacity at the second discharge was appeared to be $186\text{mA}\text{h}\text{g}^{-1}$ and at the 50th discharge it was $110\text{mA}\text{h}\text{g}^{-1}$. The irreversible capacity loss from the subsequent cycles was found to be quite large. The cycling stability was found to decrease up to 24 cycles and after that the stability is maintained. The decrease in the initial capacity loss might be due to SEI layer development at the negative electrode and other side reactions happening at the electrode surface.^[19]

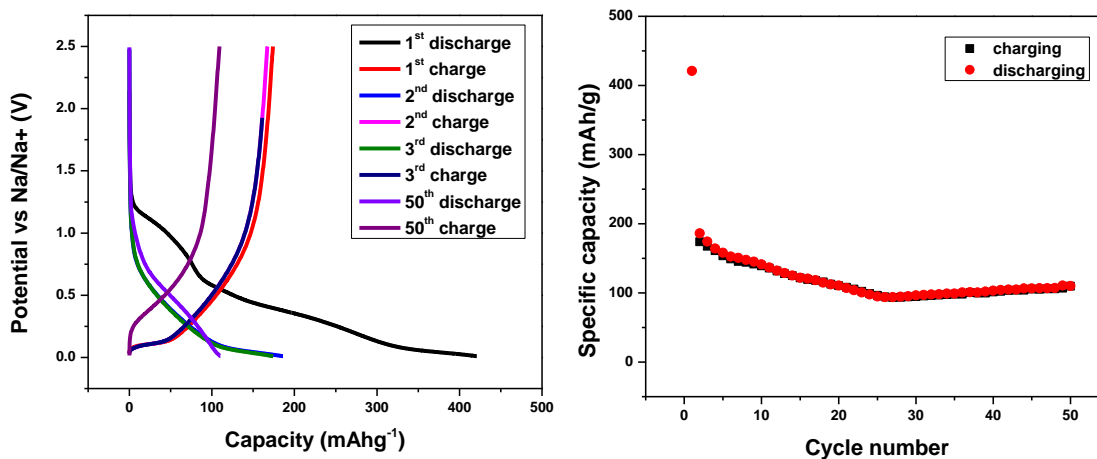


Figure 3.1.4 i) Charge-discharge profile of 50B 50R sample ii) Stability curve of 50B 50R sample up to 50 cycles

3.2 Carbon from pyrolysis of mustard seed

3.2.1 Physical and chemical characterization

Figure 3.2.1 shows the powder XRD of carbonized mustard seed. The 002 plane is observed to be shifted to lower angle when compared to the graphitic peak, indicating a larger interlayer spacing. Interlayer separation, calculated from Bragg's law was found to be 0.35 nm and in-plane crystalline size was found to be 3.42 nm calculated using Scherrer formula.

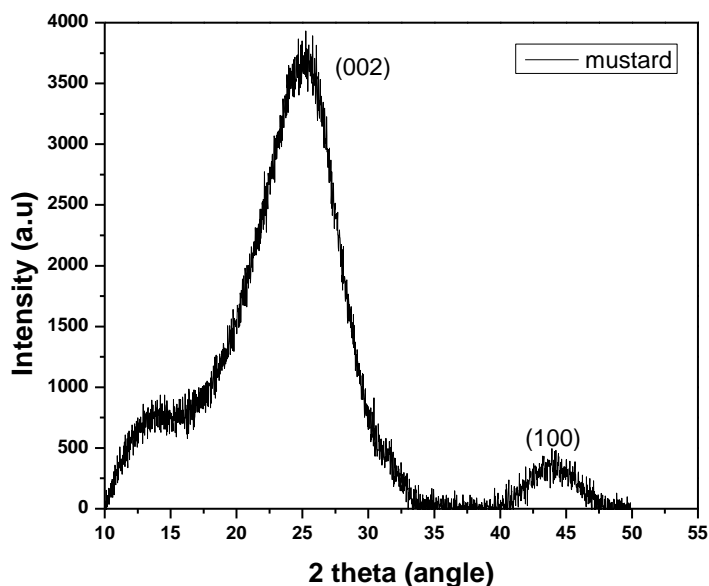


Figure 3.2.1 XRD pattern from carbonized mustard sample

Sample	XRD peak position (002)/(100)	Interplanar separation (002) (in nm)	in-plane crystallite size (100) (in nm)
Mustard	25.25 ^o / 43.92 ^o	0.35	3.42

Table 3.2.1 XRD analysis of mustard sample

Figure 3.2.2 shows the Raman spectrum of mustard sample. The Raman spectrum showed a higher intensity G-band at $\sim 1574 \text{ cm}^{-1}$ and a broad lower intensity D-band at $\sim 1369 \text{ cm}^{-1}$. The mustard sample showed I_G/I_D ratio of 1.14.

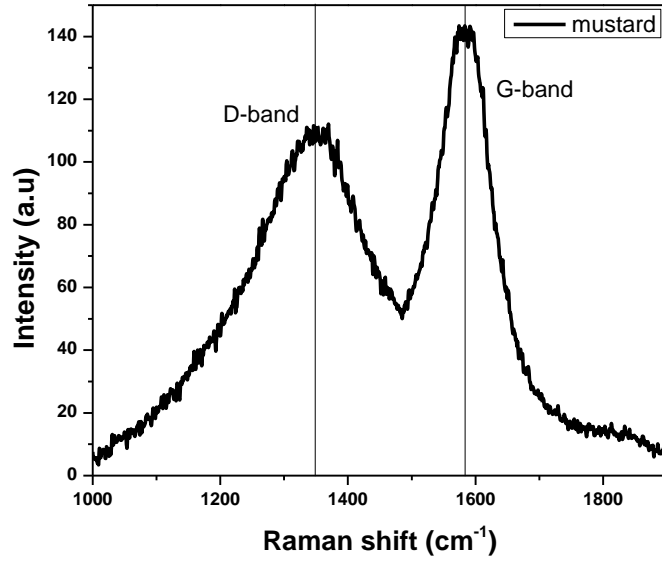


Figure 3.2.2 Raman spectrum of mustard sample

Sample	Raman G/D band position	Raman I _G /I _D ratio
Mustard	1574/1369 cm ⁻¹	1.14

Table 3.2.2 Summary of Raman analysis of mustard sample

Figure 3.2.3 shows the SEM image of mustard sample and it shows non-porous nature.

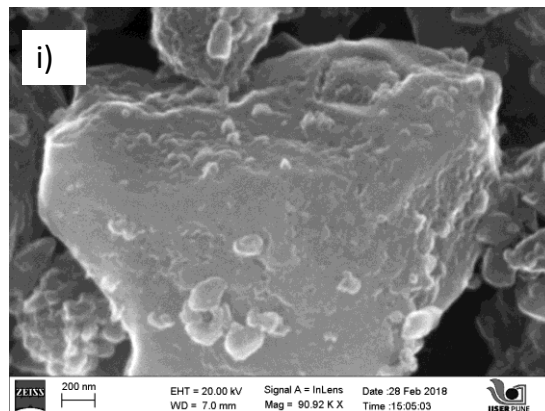


Figure 3.2.3 SEM image of mustard sample

BET surface area of mustard sample was found to be very low, $28 \text{ m}^2\text{g}^{-1}$ which is an indication of non-porous and hard nature of carbon.

Sample	BET surface area (m^2/g)
Mustard	28

Table 3.2.3 BET surface area of mustard sample

3.2.2 Electrochemical characterization

The electrochemical studies of the sodium ion storage in the carbonized mustard sample were carried out by different methods. Figure 3.2.4 shows the CV curve in the voltage range of 0.01V to 3V vs. Na/Na^+ at scan rate of 0.1 mVs^{-1} .

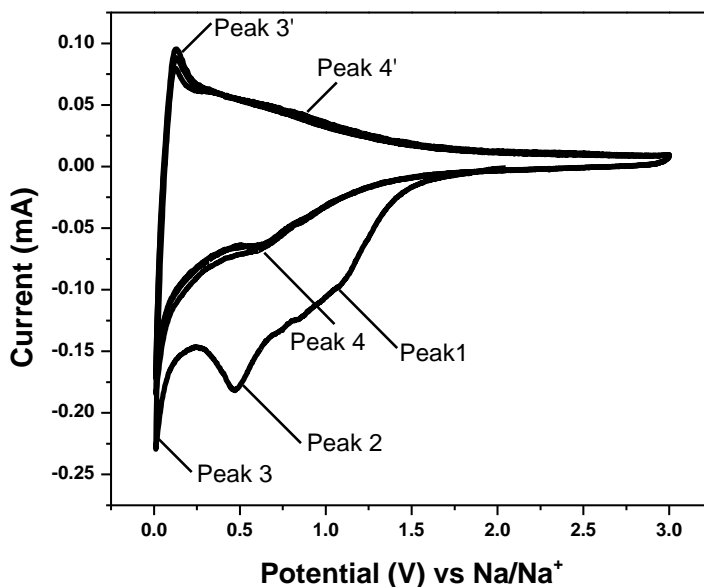


Figure 3.2.4 CV plot in the range 0.01- 3V vs. Na/Na^+ at a scan rate of 0.1 mVs^{-1}

The very broad cathodic peaks (peak 1 at 1.07V and peak 2 at 0.47V) indicate the formation of SEI layer during first cycle and it disappears during the next cycles. The cathodic peak at 0.02V (peak 3) is an indication of insertion of sodium ion into the hard carbon material. The corresponding anodic peak at 0.12V (peak 3') indicates the de-insertion of sodium ions. The additional non dominant peaks, peak 4 at 0.62V and peak 4' at 0.86V shows the intercalation and de-intercalation of sodium ion respectively into the turbostratic lattices of the material [7].

Figure 3.2.5 illustrates the electrochemical rate performance of the mustard sample as the anode material in the sodium ion half-cell configuration. The galvanostatic charge-discharge measurements were carried out at varying current densities such as 50mA g^{-1} , 100mA g^{-1} , 200mA g^{-1} , 500mA g^{-1} , 750mA g^{-1} and 1 Ag $^{-1}$ and the specific capacities obtained were 176mA $h g^{-1}$, 142mA $h g^{-1}$, 116 mA $h g^{-1}$, 93mA $h g^{-1}$, 90mA $h g^{-1}$ and 81mA $h g^{-1}$. When the current density was reduced from 1 Ag $^{-1}$ to 200mA g^{-1} the initial capacity was maintained which indicates the excellent sustainability of the material at higher current densities.

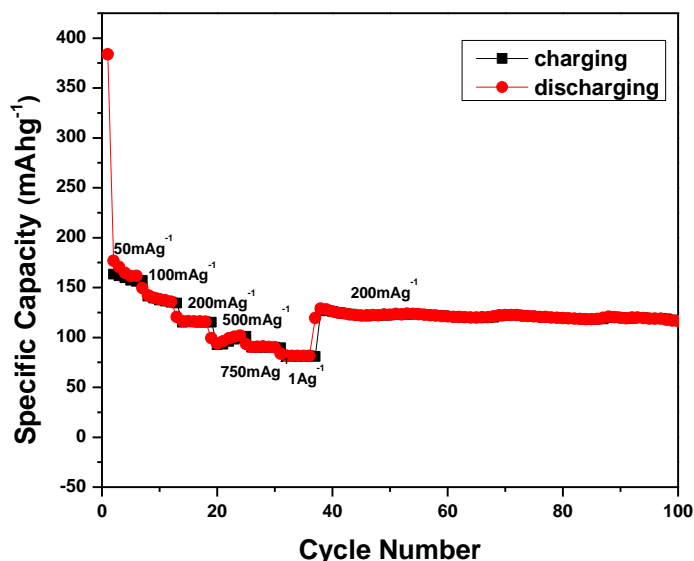


Figure 3.2.5 Electrochemical performance of mustard sample

Galvanostatic charge-discharge measurements carried out at 100mA g^{-1} are shown in figure 3.2.6.i). It shows an initial discharge capacity of 279mA g^{-1} . The irreversible loss in specific capacity from the second cycle is due to the solid electrolyte interphase development due to the electrolytic degradation or any other side reactions happening in the electrode surface. The sloping region from 1.2V to 0.5V is an indication of the development of SEI layer on the negative electrode. The reversible capacity of the sample was found to be 112mA g^{-1} . The typical sodium ion insertion happens by two different mechanisms. The sloping region and plateau region are two regions where sodium insertion occurs. Intercalation of the sodium ions in between the graphene planes leads to the sloping region and the adsorption of ions in the nanopores and nanovoids of the material leads to the plateau region which at very low voltage ^[20]. In the remaining cycles, the curves are maintained similar to the second charge-discharge cycle. The cycling stability over 270 cycles for the charge-discharge measurements are shown in figure 3.2.6.ii). The capacity is retained up to 270 cycles, showing good cycling stability of the material. The material exhibited high coulombic efficiency.

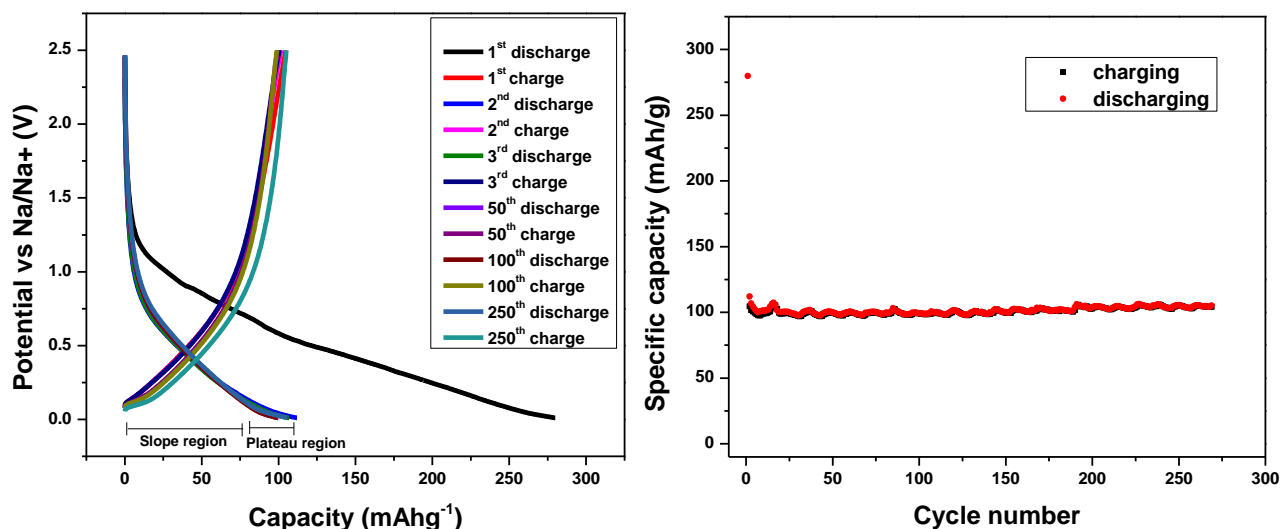


Figure 3.2.6 i) Charge – discharge profile of mustard sample ii) Stability curve of mustard sample up to 270 cycles

Chapter 4

CONCLUSION AND FUTURE ASPECTS

Carbonized products of bagasse, melamine – formaldehyde resin and its composites were successfully synthesized and the physical and chemical characterizations were performed using different techniques. Galvanostatic charge – discharge measurements were performed for the 50:50 ratio of bagasse and resin sample. The 50B 50R sample showed an initial discharge capacity of 421mAhg^{-1} and second discharge capacity was found to be 186mAhg^{-1} . Electrochemical characterizations such as CV, impedance measurements, charge-discharge measurement and rate performance of the 50B 50R sample needs to be completed. Electrochemical characterizations of the other four samples needs to be performed for a comparative study. Also, varying the pyrolysis temperature greater than 800°C to find the change in morphology and structure of different samples is of interest.

The carbonized product of mustard seeds were analyzed by physical, chemical and electrochemical characterization techniques. The sample showed a capacity of 112mAhg^{-1} with excellent cycling stability. Further studies needs to be performed to improve the capacity of the material.

REFERENCES

1. History of Batteries: A Timeline, 2014, www.upsbatterycenter.com/blog/historybatteries-timeline
2. J. R. Dahn, D.A.Stevens, *Journal of the Electrochemical Society*, **2000**, 147, 1271-1273.
3. N. Nitta, F. Wu, J. T. Lee, G. Yushin, *Materials Today*, **2015**, 18, 5.
4. M. Wahid, D. Puthusseri, Y. Gawli, N. Sharma, S. Ogale, *ChemSusChem*, **2018**, 11,1–22.
5. J.Y Hwang, S.T. Myung, Y.K. Sun, *Chem.Soc.Rev.*, **2017**,46, 3529—3614.
6. N. Yabuuchi, K. Kubota, M. Dahbi, S. Komaba, *Chem.Rev.*, **2014**, 114, 11636–11682.
7. M. Wahid, Y. Gawli, D. Puthusseri, A. Kumar, M.V. Shelke, S. Ogale, *ACS Omega*, **2017**, 2, 3601–3609.
8. E. Irisarri, A. Ponrouch, M. R. Palacin, *J. Electrochem. Soc.* **2015**, 162, 2476-2482.
9. J. R. Dahn, Tao Zheng, Yinghu Liu, J. S. Xue *Science* **1995**, 270, 590-593.
10. L. Fan, Q. Liu, S. Chen, Z. Xu, B. Lu, *Adv. Energy Mater.* **2017**, 7, 1602778.
11. Z. Jian, S. Hwang, Z. Li, A. S. Hernandez, X. Wang, Z. Xing, D. Su, X. Ji, *Adv. Funct. Mater.* **2017**, 1700324.
12. M. Wahid, D. Puthusseri, D. Phase, S. Ogale, *Energy Fuels* **2014**, 28, 4233–4240.
13. Z. H. Wang, L. Qie, L. X. Yuan, W. X. Zhang, X. L. Hu, Y. H. Huang, *Carbon*, **2013**, 55, 328.
14. B. Friedel, S. G. Weber, *Small* **2006**, 2, 859 – 863.

15. K. Krishnamoorthy, M. Veerapandian, K. Yun, S. Kim, *Carbon*, **2013**, 53, 38-49.
16. S.Komaba, W. Murata, T. Ishikawa, N. Yabuuchi, T. Ozeki, T.Nakayama, A.Ogata, K. Gotoh, K. Fujiwara, *Adv. Funct. Mater*, **2011**, 21, 3859–3867.
17. P.Giura, N. Bonini, G. Creff, J.B Brubach, P. Roy, M.Lazzeri, *Phys. Rev. B: Condens. Matter Mater. Phys*, **2012**, 86, 1–5.
18. K. Tang, L. J. Fu, R. J. White, L. H. Yu, M. M. Titirici, M. Antonietti, J. Maier, *Adv. Energy Mater.*, **2012**, 2, 873.
19. D. H. Wang, Y. Hu, J. J. Zhao, L. L. Zeng, X. M. Tao, W. Chen, *J. Mater. Chem. A*, **2014**, 2, 17415.
20. P.G. Bruce, S.A. Freunberger, L.J. Hardwick, J.M. Tarascon, *Nat. Mater.*, **2012**, 11, 19–29.